 CMES, vol.3, no.1, pp.129-145, 2002

Generation-Phase Simulation of Dynamic Crack Bifurcation Phenomenon Using Moving Finite Element Method Based on Delaunay Automatic Triangulation

T. Nishioka [1] , J. Furutuka[1], S. Tchouikov[1] and T. Fujimoto[1]

Abstract The governing condition of dynamic crack bifurcation phenomena had not been fully elucidated until our recent experimental studies. We found from the experimental results that the energy flux per unit time into a propagating crack tip or into a fracture process zone governs the crack bifurcation. Regarding the numerical simulation of dynamic crack bifurcation, to the authors' knowledge, no accurate simulations have been carried out, due to several unresolved difficulties. In order to overcome the difficulties, for the analysis of dynamic crack bifurcation, we developed a moving finite element method based on Delaunay automatic triangulation. Using the moving finite element method, the generation phase simulation was carried out, based on the experimentally recorded fracture histories by an ultra-high speed camera. To evaluate fracture parameters for shortly branched cracks, a switching method of the path independent dynamic J integral was also developed. The simulated results agree excellently with those of the experiment. Furthermore, the numerical simulation revealed detailed variations of various fracture parameters before and after the crack bifurcation.

keyword: Dynamic fracture, dynamic crack bifurcation, dynamic crack branching, Delaunay triangulation, moving element method, automatic mesh generation, dynamic J integral, path independent integral.

1 Introduction

The prediction of brittle fracture path is extremely important for safety design of structures. Branched cracks are often observed in brittle materials and structures. Many researchers have attempted to elucidate the mechanism of crack branching. However the governing condition of dynamic crack branching had not been fully elucidated until our recent experimental studies [Nishioka, Kishimoto, Ono and Sakakura (1999a, 1999b)]. Thus, dynamic crack bifurcation had remained as one of the most important unsolved problems in dynamic fracture mechanics. In our recent experimental studies [Nishioka, Kishimoto, Ono and Sakakura (1999a, 1999b)], we investigated dynamic crack branching phenomena in Homalite-911 and Homalite-100. The experimental results revealed that the energy flux per unit time into a propagating crack tip or into a fracture process zone governs the dynamic crack bifurcation.

Regarding the numerical simulation of dynamic crack bifurcation, to the authors' knowledge, no accurate simulations have been carried out, due to several unresolved difficulties. Main reasons of these difficulties may be listed as follows:

(1) Moving singularities at the tips of dynamically propagating cracks should be treated accurately. The ordinary numerical methods cannot treat the fast moving singularities.

(2) When a propagating crack bifurcates, the material point at the site of crack branching instantaneously separates into at least three parts. In the ordinary numerical models with nodal release techniques, this sudden unloading process often produces spurious oscillations.

(3) Branched crack paths are generally complicated. Automatic mesh generations for these non-self-similar fast fracture phenomena are extremely difficult.

(4) Since the branched crack tips immediately after the bifurcation locate extremely closely, it is difficult to evaluate fracture parameters such as the dynamic J integral [Nishioka and Atluri (1983)] and dynamic stress intensity factors for the branched short cracks.

In previous studies, the authors [Nishioka, Tokudome, Kinoshita and Nishida (1998); Nishioka, Tokudome and Kinoshita (2001)] developed a moving finite element method based on Delaunay automatic triangulation. This moving finite element method made it possible to establish the numerical prediction technology for dynamically

[1] Simulation Engineering Laboratory, Dept. of Ocean Mechanical Enginering, Kobe University of Mercantile Marine, Higashinada-Ku, Kobe, 658-0022, Japan

kinking and curving fracture phenomena under impact loads.

In this study, to overcome the difficulties in the numerical simulation for dynamically branching fracture phenomena, we develop a numerical simulation method using the moving finite element method based on Delaunay automatic triangulation [Sloan and Houlsby (1984) and Taniguchi (1992)].

Using this moving finite element method, we make it possible to carry out the generation phase simulation [Kanninen (1978)] for the experimentally observed phenomenon of dynamic crack bifurcation. In the generation phase simulation, the phenomenon is regenerated in the computational models using the experimentally recorded fracture history. In order to evaluate the dynamic J integral values for dynamically branching cracks, a switching of the path independent dynamic J integral is also developed.

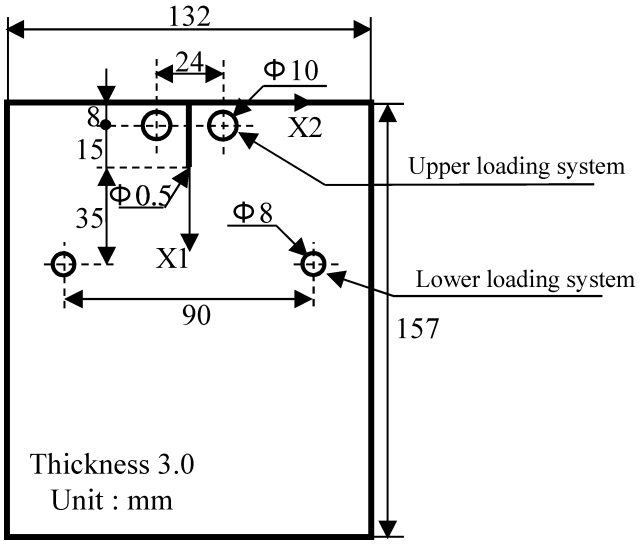

Figure 1 : Specimen geometry

2 Experimental Measurement of Dynamic Crack Bifurcation

In the experiments [Nishioka, Kishimoto, Ono and Sakakura (1999a, 1999b)], transparent materials, Homalite-100 and Homalite-911 were used. In this paper, we carry out the generation phase simulation for a Homalite-911 specimen. The material properties of Homalite-911 are as follows: Young's modulus E=2.07GPa, Poisson ratio ν=0.420 and mass density ρ=1310kg/m^3. The geometry of a typical specimen used for fast crack branching test is shown in Fig. 1. The initial crack (notch) length was set as 23mm from the upper end of the specimen.

Two sets of displacement-controlled loads were applied to the specimen through two pairs of loading pins (one pair at X_1=8mm and X_2=$\pm$12mm and other pair at X_1=58mm and X_2=$\pm$45mm). First, the lower loading system was applied and held constant (see Fig. 2). Then the upper loading system was gradually applied by the L shape jigs as depicted in Fig. 2, until dynamic crack propagation occurs. The lower loading system produces a strong tensile stress field to supply enough energy into the propagating crack tip for crack branching. The crack branching occurs near the lower loading line. Thus, the X_1 position of the lower loading system controls the site of the crack bifurcation. Dynamic fracture started at the upper load of 68.6N under the lower load of 1822.8N. In

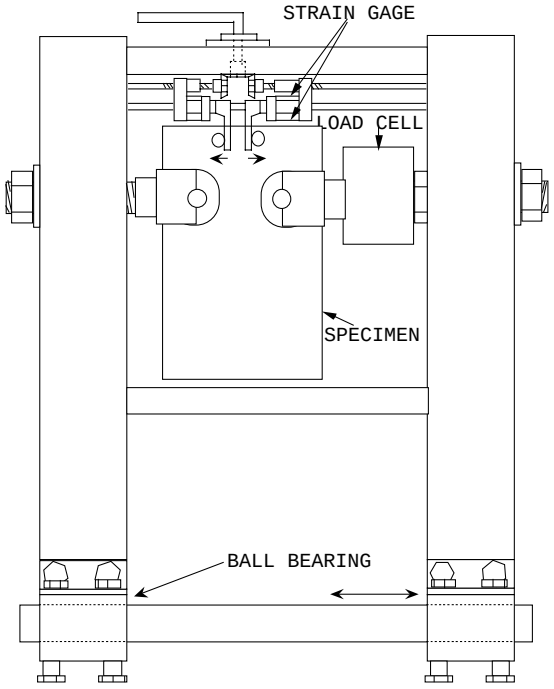

Figure 2 : Loading Equipment

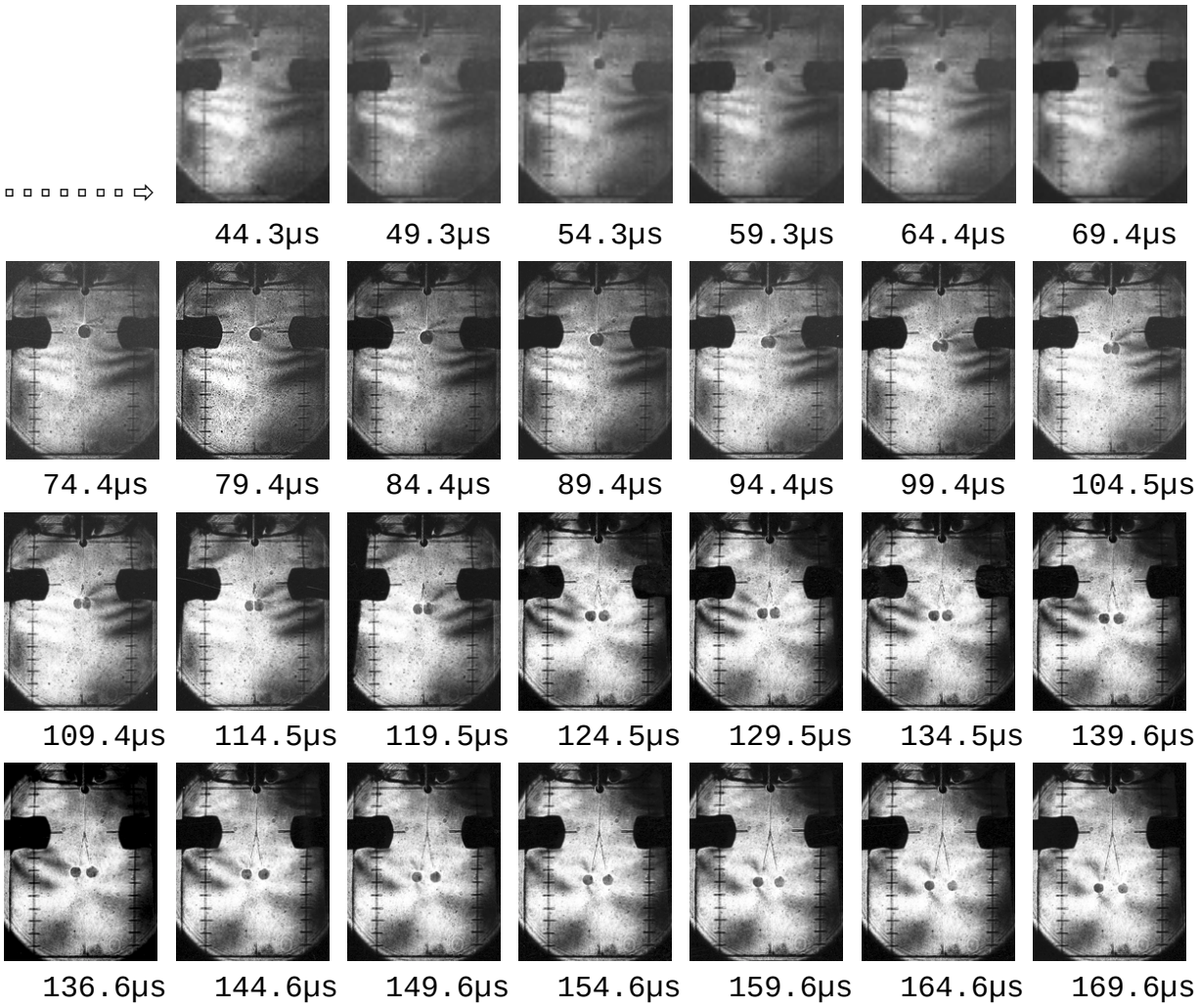

Figure 3 : High-speed photographs of dynamic crack bifurcation phenomenon

the experiments, using a high-speed camera (the maximum framing rate: two million frames per second), high-speed photographs of the caustic patterns were recorded. A series of high-speed photographs of the caustic patterns in the specimen of Homalite-911 is shown in Fig. 3. The framing rate used was about two hundred thousand frames per second. Thus the frame intervals were about 5 μs.

The history of crack propagation in this specimen is shown in Fig. 4. The crack-tip positions of the main crack and branched cracks were measured from the upper end of the specimen. It is seen that the branched cracks propagated almost completely symmetrically. The crack branching occurred at time t_b=79.4 μs after the initiation of dynamic fracture from the initial crack. The straight crack length at the onset of dynamic crack branching was 59.54mm from the upper end of the specimen. The initial crack branching angle was about 25.2 $^\circ$.

A polynomial curve is fitted for the main crack as well as for each branched crack (see solid lines in Fig. 4). Then differentiating the polynomials with time, the crack velocities were determined and depicted in Fig. 5. As seen from the figure, the crack velocities immediately before and after the crack bifurcation were the same. Also, the crack velocities were almost constant. The average crack velocities were about 450 m/s.

3 Moving Finite Element Method for Dynamic Crack Bifurcation Phenomenon

To simulate crack propagation by the finite element method, two different concepts of computational model-

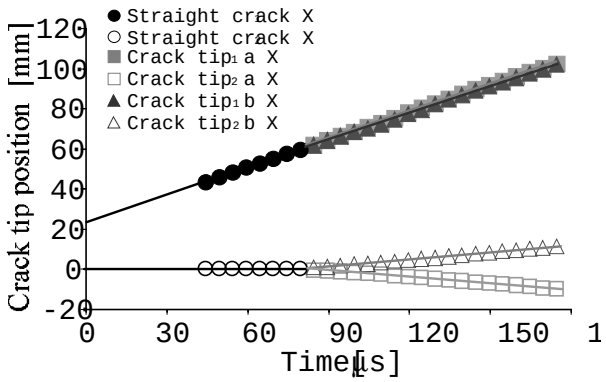

Figure 4 : Crack propagation history

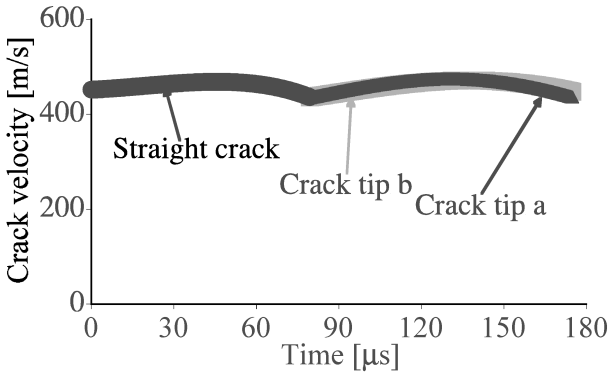

Figure 5 : Crack velocity variations

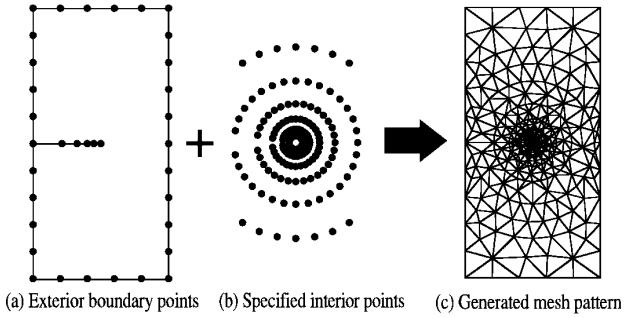

Figure 6 : An example of mesh generation

ing can be considered, i.e. (i) the stationary element procedure (or fixed element procedure), and (ii) the moving element procedure, as reviewed by Nishioka and Atluri (1986), and Nishioka (1994, 1997). For dynamic crack propagation problems, the fixed finite element procedure has the following severe disadvantages:

(1) The boundary conditions in front of and behind the propagating crack tip cannot be satisfied exactly.

(2) The violation of the boundary conditions produces spurious numerical error waves in the model.

(3) The fixed mesh pattern may not fit with the actual fracture paths.

To overcome the aforementioned difficulties, Nishioka and coworkers have developed various types of moving finite element method. These were reviewed and summarized by Nishioka and Atluri (1986) and Nishioka (1994, 1997). Recently the concept of the moving finite element method was extended by Nishioka, Tokudome, Kinoshita and Nishida (1998); Nishioka, Tokudome, Kinoshita (2001) to dynamically curving and kinking fracture problems using the modified Delaunay automatic triangulation [Taniguchi (1992)].

In this study, we further extend the moving finite element method based on Delaunay automatic triangulation to dynamic crack branching problems.

3.1 Automatic mesh generation for dynamically propagating and branching cracks

In the modified Delaunay triangulation, only exterior and interior boundary points and specified interior points (if they are necessary) are required for automatic mesh generation. Figure 6 shows an example of mesh generation for a plate with an edge crack. The specified points at the boundaries are shown in Fig. 6(a). To distinguish the upper and lower crack surfaces, the coordinates of the upper and lower crack surfaces are shifted by infinitesimally small distances $\pm\varepsilon$ toward the perpendicular direction to the crack surfaces. Thus, the crack is opened by 2ε. Due to the stress singularity at the crack tip, the specified interior points are placed around the crack tip as depicted in Fig. 6(b). Then the mesh pattern in Fig. 6(c) is automatically generated using the exterior boundary points and the specified interior points.

In this paper, the moving finite element method based on Delaunay automatic triangulation is extended for dynamic crack branching, as shown in Fig. 7. The group of the specified interior points around the propagating crack tip translates in each time step for which crack growth occurs. When the crack bifurcation occurs, the group of the specified interior points is separated for the branched crack tips. In each time step, the previous crack tip point breaks into two nodal points, except three points for two crack branching. Thus at least four degrees of freedom per crack tip should be increased in each crack increment.

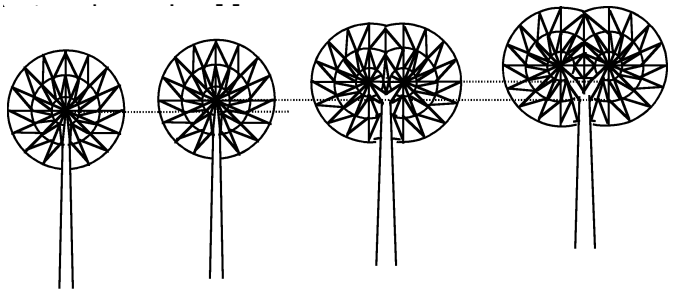

Figure 7 : Moving elements around dynamically branching crack tips

The crack-tip always remains at the center of the group of the moving elements throughout the analysis even for complicated crack propagation.

3.2 Time integration method

In this study, the Newmark method is used for the time integration of the finite element equations of motion. At a generic time step *n*, the final simultaneous equations to be solved are expressed as

$$(a_0[M]^{(n)} + [K]^{(n)})\{Q\}_n^{(n)} =$$

$$\{F\}_n^{(n)} + [M]^{(n)}(a_0\{Q\}_{n-1}^{(n)} + a_2\{\dot{Q}\}_{n-1}^{(n)} + a_3\{\ddot{Q}\}_{n-1}^{(n)}) \quad (1)$$

where $\{Q\}, \{\dot{Q}\}, \{\ddot{Q}\}$ are the global vectors of nodal displacements, nodal velocities and nodal accelerations, respectively. The subscripts n and $n-1$ denote the quantities at the present time step n and at the previous time step $n-1$, respectively, while the superscript (n) denotes the quantities in the mesh pattern of the present time step *n*. *[M], [K],* $\{F\}$ are the mass matrix, the stiffness matrix and the load vector, respectively. The coefficients $a_0 \sim a_3$ are the parameters in the Newmark method (see Eq. (4)).

After solving Eq. (1) for the nodal displacements at the present time step, the nodal velocities and accelerations can be evaluated by the following equations:

$$\{\ddot{Q}\}_n^{(n)} = a_0(\{Q\}_n^{(n)} - \{Q\}_{n-1}^{(n)}) - a_2\{\dot{Q}\}_{n-1}^{(n)} - a_3\{\ddot{Q}\}_{n-1}^{(n)}, \quad (2)$$

$$\{\dot{Q}\}_n^{(n)} = \{\dot{Q}\}_{n-1}^{(n)} + a_6\{\ddot{Q}\}_{n-1}^{(n)} + a_7\{\ddot{Q}\}_n^{(n)}. \quad (3)$$

The coefficients are given as

$$a_0 = \frac{1}{\beta(\Delta t_n)^2},\ a_1 = \frac{\delta}{\beta\Delta t_n},\ a_2 = \frac{1}{\beta\Delta t_n},\ a_3 = \frac{1}{2\beta} - 1,$$
$$a_4 = \frac{\delta}{\beta} - 1, a_5 = \frac{\Delta t_n}{2}\left(\frac{\delta}{\beta} - 2\right),\ a_6 = \Delta t_n(1-\delta),$$
$$a_7 = \delta\Delta t_n \quad (4)$$

where Δt_n is the time increment at the present time step. In this study, the Newmark's parameters are chosen to be β*=1/4* and δ*=1/2* to fulfill the unconditionally stable condition [Bathe and Wilson (1976)].

3.3 Mapping of solution fields in the previous mesh onto those in the present mesh

As explained in the previous subsections, in the moving finite element method, the moving-mesh and remeshing procedures are used (see Fig. 7). To use the Newmark time integration scheme for the moving finite element method, the previous solution fields for the current mesh pattern are needed, i.e., $\{Q\}_{n-1}^{(n)}, \{\dot{Q}\}_{n-1}^{(n)}, \{\ddot{Q}\}_{n-1}^{(n)}$ (see the right-hand side of Eq. (1)). This means that the mapping of the solution fields in the previous mesh onto those in the present mesh is needed.

In this subsection, the detailed procedures for constructing $\{Q\}_{n-1}^{(n)}, \{\dot{Q}\}_{n-1}^{(n)}, \{\ddot{Q}\}_{n-1}^{(n)}$ from the previous solution fields in the previous mesh $\{Q\}_{n-1}^{(n-1)}, \{\dot{Q}\}_{n-1}^{(n-1)}$, and $\{\ddot{Q}\}_{n-1}^{(n-1)}$ are given. For the mapping of the solution fields in the previous mesh onto those in the present mesh, we have developed the following two procedures:

3.3.1 Searching an element in the previous mesh for a new nodal point

Let us consider a newly created nodal point in the present mesh as the *p*th node. The program searches the element in the previous mesh in which the new *p*th node is included, as shown in Fig. 8. The triangles A_1,$A_2$and A_3 are calculated by the following determinants:

$$A_1 = \frac{1}{2}\begin{vmatrix} 1 & x_p & y_p \\ 1 & x_2 & y_2 \\ 1 & x_3 & y_3 \end{vmatrix}, A_2 = \frac{1}{2}\begin{vmatrix} 1 & x_p & y_p \\ 1 & x_3 & y_3 \\ 1 & x_1 & y_1 \end{vmatrix}, A_3 = \frac{1}{2}\begin{vmatrix} 1 & x_p & y_p \\ 1 & x_1 & y_1 \\ 1 & x_2 & y_2 \end{vmatrix} \quad (5)$$

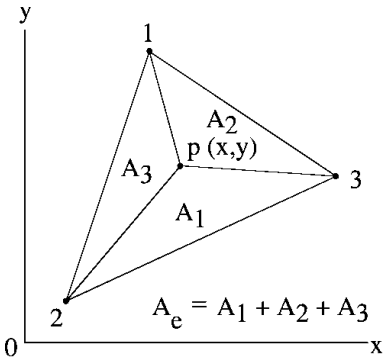

Figure 8 : A New nodal point in the previous mesh

where x_p and y_p are the coordinates of the point p, and x_i and y_i *(i=1,2,3)* are the coordinates of the nodes 1, 2 and 3.

It can easily be judged whether the pth node is inside of the element or not. If A_1, A_2 and A_3 are all positive, the pth node is inside of the element, while it is outside if any of A_1, A_2 or A_3 is negative.

3.3.2 Creating nodal quantities for the new nodal point

Once the old element including the new pth node is found, the area coordinates of the pth node can be calculated by

$$\xi_{1p} = A_1/A_e, \quad \xi_{2p} = A_2/A_e, \quad \xi_{3p} = A_3/A_e \tag{6}$$

where $A_e$is the area of the element. Since in this paper we use linear triangle elements, the shape functions N_i of the point p are given by

$$N_i = \xi_{ip} \quad (i = 1,2,3). \tag{7}$$

Using these shape functions, the nodal displacements, nodal velocities and nodal accelerations in the x and y directions can be constructed for the new pth node as follows:

$$(u_p)_{n-1}^{(n)} = \sum_{i=1}^{3} N_i^{(n-1)}(\xi_{1p},\xi_{2p},\xi_{3p})(u_i)_{n-1}^{(n-1)};\ (p = 1,2\ldots N) \tag{8a}$$

$$(v_p)_{n-1}^{(n)} = \sum_{i=1}^{3} N_i^{(n-1)}(\xi_{1p},\xi_{2p},\xi_{3p})(v_i)_{n-1}^{(n-1)};\ (p = 1,2\ldots N) \tag{8b}$$

$$(\dot{u}_p)_{n-1}^{(n)} = \sum_{i=1}^{3} N_i^{(n-1)}(\xi_{1p},\xi_{2p},\xi_{3p})(\dot{u}_i)_{n-1}^{(n-1)};\ (p = 1,2\ldots N) \tag{9a}$$

$$(\dot{v}_p)_{n-1}^{(n)} = \sum_{i=1}^{3} N_i^{(n-1)}(\xi_{1p},\xi_{2p},\xi_{3p})(\dot{v}_i)_{n-1}^{(n-1)};\ (p = 1,2\ldots N) \tag{9b}$$

$$(\ddot{u}_p)_{n-1}^{(n)} = \sum_{i=1}^{3} N_i^{(n-1)}(\xi_{1p},\xi_{2p},\xi_{3p})(\ddot{u}_i)_{n-1}^{(n-1)};\ (p = 1,2\ldots N) \tag{10a}$$

$$(\ddot{v}_p)_{n-1}^{(n)} = \sum_{i=1}^{3} N_i^{(n-1)}(\xi_{1p},\xi_{2p},\xi_{3p})(\ddot{v}_i)_{n-1}^{(n-1)};\ (p = 1,2\ldots N) \tag{10b}$$

where N denotes the total number of new nodes created in the remeshed zone including the moving element zone.

The presently developed moving finite element method based on Delaunay automatic triangulation is very efficient and powerful to simulate complicated dynamic fracture phenomena such as dynamic crack bifurcation. For such complicated fracture simulations, the readers can also confer other recently developing techniques [Kim and Atluri (2000), Chen, Hu and Chen (2000), Abraham (2000), Ching and Batra (2001)].

4 Contact and Non-Contact Boundary Conditions for Loading Points

Since in general the L shape jigs used in the loading device (see Fig. 2) can "push" the loading pins but not

"pull", the fixed boundary conditions at the upper loading points in the numerical analysis may lead to a spurious deformation behavior of the specimen. Thus, account should be taken of the possibility of lack of contact of the L shape jigs with the loading pins, at various instants of time. For this kind of problem, Nishioka and coworkers were the first to introduce the contact/non-contact boundary conditions to three-point bend specimens [Nishioka, Perl and Atluri (1983)], and to double cantilever beam specimens [Nishioka and Atluri (1982)]. From the numerical results for the three-point bend fracture test [Nishioka, Perl and Atluri (1983)], it was found that the specimen was periodically not in contact with either the impact rod or the supports; i.e. the specimen periodically became a free-flying object.

In the present study, the contact/non-contact boundary conditions are also employed in the numerical simulations. The contact/non-contact boundary conditions are incorporated in the program as follows.

We designate the nodal forces at the left and right lower loading points, as $F_{Y\alpha}$ *(*α*= l, r)* (the global Y direction coincides with the X_2 direction depicted in Fig. 1), and the corresponding displacement components at those points as v_α *(*α*= l, r)*. Then, those nodal forces and displacements in the next time step $(n+1)$ are predicted by

$$(F_{Y\alpha})_{n+1} = (F_{Y\alpha})_n + \frac{((F_{Y\alpha})_n - (F_{Y\alpha})_{n-1})}{\Delta t_n}\Delta t_{n+1} : (\alpha = l, r) \tag{11}$$

and

$$(v_\alpha)_{n+1} = (v_\alpha)_n + (\dot{v}_\alpha)_n \Delta t_{n+1} : (\alpha = l, r). \tag{12}$$

The initial conditions at those points are given by

$$(v_\alpha)_0 = (\overline{v}_\alpha)_0, (\dot{v}_\alpha)_0 = (\dot{\overline{v}}_\alpha)_0, (\ddot{v}_\alpha)_0 = (\ddot{\overline{v}}_\alpha)_0 : (\alpha = l, r) \tag{13}$$

where the upper bars denote prescribed values.

A negative value of $(F_{Yl})_{n+1}$ and a positive value of $(F_{Yr})_{n+1}$ indicate that the loading pins will be pushed by the L shape jigs. Thus, the contact condition at each point continues if the sign of the corresponding predicted nodal force at the next time step $(n+1)$ (see Eq. (11)) remains unchanged. The non-contact condition at each point occurs if the corresponding value of $(F_{Y\alpha})_{n+1}$ *(*α*= l, r)* becomes zero or of the different sign.

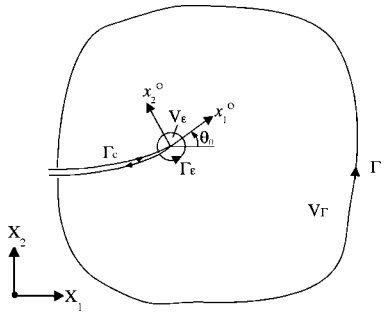

Figure 9 : Definition of integral paths

When the non-contact condition is predicted, that point is set as free at the next time step. The movement of that point is calculated by the simulation. The free state continues if the sign of the gap $((v_\alpha)_{n+1} - (\overline{v}_\alpha)_{n+1})$ *(*α*= l, r)* remains unchanged from the current time step. Then, recontact condition occurs if the gap $((v_\alpha)_{n+1} - (\overline{v}_\alpha)_{n+1})$ *(*α*= l, r)* is predicted as zero or of the different sign.

Although in [Nishioka, Perl and Atluri (1983)] the time increment was subdivided whenever the transition to the non-contact or re-contact condition was predicted to occur prior to the time of the next step, in this study a sufficiently small constant time increment is always used throughout the simulation.

5 Evaluation of Dynamic Fracture Mechanics Parameters for a Single Crack

To evaluate various fracture mechanics parameters for a crack subject to impact stress wave loading, and for a dynamically kinking as well as dynamically curving crack, the path independent dynamic J integral derived by Nishioka and Atluri (1983) is used.

5.1 Path independent dynamic J integral

The static J integral [Rice (1968)]has played an important role in *static fracture mechanics*. From the theoretical and computational points of view, the static J integral has the following salient features: (i) it physically represents the energy release rate; (ii) it has the property of the path-independent integral, which gives a unique value for an arbitrary integral path surrounding the crack tip; (iii) it

can be related to the stress intensity factors by arbitrarily shrinking the integral path to the crack tip.

In the case of *dynamic fracture mechanics*, Nishioka and Atluri (1983)have derived the dynamic J integral (J') which has the aforementioned three features. We consider a dynamically propagating crack in an elastic solid as shown in Fig. 9. The global-axis components of the dynamic J integral can be expressed by

$$J'_k = \lim_{\Gamma_\varepsilon \to 0} \int_{\Gamma_\varepsilon} [(W+K)n_k - t_i u_{i,k}] dS \tag{14a}$$

$$= \lim_{\Gamma_\varepsilon \to 0} \left\{ \int_{\Gamma+\Gamma_c} [(W+K)n_k - t_i u_{i,k}] dS + \int_{V_\Gamma - V_\varepsilon} [(\rho \ddot{u}_i - f_i) u_{i,k} - \rho \dot{u}_i \dot{u}_{i,k}] dV \right\} \tag{14b}$$

where u_i, t_i, f_i, n_k and ρ denote the displacement, traction, body force, outward direction cosine, and mass density, respectively. W and K are the strain and kinetic energy densities, respectively, and $()_{,k} = \partial( )/\partial X_k$. The integral paths are defined in Fig. 9. Γ_ε, Γ, and Γ_c denote a near-field path, far-field path and crack surface path, respectively. V_Γ is the region surrounded by Γ, while V_ε is the region surrounded by Γ_ε.

In most numerical analyses, the dynamic J integral (J') can be evaluated by the following expression after taking the limit $\Gamma_\varepsilon \to 0$:

$$J'_k = \int_{\Gamma+\Gamma_c} [(W+K)n_k - t_i u_{i,k}] dS + \int_{V_\Gamma} [(\rho \ddot{u}_i - f_i) u_{i,k} - \rho \dot{u}_i \dot{u}_{i,k}] dV. \tag{15}$$

The crack-axis components of the dynamic J integral can be evaluated by the following coordinate transformation:

$$J'^0_\ell = \alpha_{lk}(\theta_0) J'_k. \tag{16}$$

where α_{lk} is the coordinate transformation tensor and θ_0 is the angle between the global axis X_1 and the crack axis x^0_1. The tangential component of the dynamic J integral J'^0_1 corresponds to the rate of change in the potential energy per unit crack extension, namely, the dynamic energy release rate.

The dynamic J integral can be related to the instantaneous stress intensity factors for the elastodynamically propagating crack with velocity C, as in [Nishioka and Atluri (1983)]:

$$J'^0_l = \frac{1}{2\mu}\{A_I(C)K_I^2 + A_{II}(C)K_{II}^2 + A_{III}(C)K_{III}^2\} \tag{17}$$

$$J'^0_2 = -\frac{A_{IV}(C)}{\mu} K_I K_{II} \tag{18}$$

where μ is the shear modulus, and $A_I(C) - A_{IV}(C)$ are functions of crack velocity C and given in Nishioka and Atluri (1983).

The salient features of the dynamic J integral can be summarized as follows:

(i) It physically represents the dynamic energy release rate G [Nishioka and Atluri (1983)].

(ii) For the far-field path, it has the property of the path-independent integral [Nishioka and Atluri (1983)].

(iii) For the near-field path, it is practically invariant with the shape of the infinitesimal near-field path [Nishioka (1994)].

(iv) The dynamic J integral includes the static J integral for elastostatic fracture problems.

(v) The near-field path can be taken as the boundary of a fracture process zone (if it is known a priori).

5.2 Determination of mixed-mode stress intensity factors from the dynamic J integral components

To accurately evaluate the inplane mixed-mode stress intensity factors from the dynamic J integral values, the component separation method [Nishioka (1994)] was proposed. The formulae of the component separation method are expressed by using the global components of the dynamic J integral as

$$K_I = \delta_I \left\{ \frac{2\mu\beta_2(J'_1 \cos\theta_0 + J'_2 \sin\theta_0)}{A_I(\delta_I^2\beta_2 + \delta_{II}^2\beta_1)} \right\}^{1/2} \tag{19a}$$

$$K_{II} = \delta_{II} \left\{ \frac{2\mu\beta_1(J'_1 \cos\theta_0 + J'_2 \sin\theta_0)}{A_{II}(\delta_I^2\beta_2 + \delta_{II}^2\beta_1)} \right\}^{1/2} \tag{19b}$$

where δ_I and δ_{II} are the mode I and mode II crack opening displacements at a point near the crack tip, and $A_I(C), A_{II}(C)$ are functions of crack velocity and given in [Nishioka and Atluri (1983)]. θ_0 is the angle of crack direction measured from the global axis X_1.

If the energy release rate G or the crack-axis component is obtained by Eq. (16), the following formulae are also very useful:

$$K_I = \delta_I \left\{ \frac{2\mu J_1'^0 \beta_2}{A_I(\delta_I^2\beta_2 + \delta_{II}^2\beta_1)} \right\}^{1/2} = \delta_I \left\{ \frac{2\mu G \beta_2}{A_I(\delta_I^2\beta_2 + \delta_{II}^2\beta_1)} \right\}^{1/2} \tag{20a}$$

$$K_{II} = \delta_{II} \left\{ \frac{2\mu J_1'^0 \beta_2}{A_{II}(\delta_I^2\beta_2 + \delta_{II}^2\beta_1)} \right\}^{1/2} = \delta_{II} \left\{ \frac{2\mu G \beta_2}{A_{II}(\delta_I^2\beta_2 + \delta_{II}^2\beta_1)} \right\}^{1/2} \tag{20b}$$

The component separation method has the following features: (i) mixed-mode stress intensity fractors can be evaluated by ordinary non-singular elements, and (ii) the signs of K_I and K_{II} are automatically determined by the signs of δ_I and δ_{II}, respectively.

6 Switching Method of Path Independent Dynamic J Integral for Branched Crack Tips

The close proximity of the crack tips immediately after crack bifurcation make it very difficult to accurately evaluate fracture parameters such as the dynamic J integral and dynamic stress intensity factors. To overcome this difficulty, a switching method of the path independent dynamic J integral is derived as follows:

$$J_k' = \int_{\Gamma+\Gamma_c} [(W+K)n_k - t_i u_{i,k}] s dS + \int_{V_\Gamma - V_\varepsilon} [\{(\rho\ddot{u}_i - f_i)u_{i,k} - \rho\dot{u}_i\dot{u}_{i,k}\}s + \sigma_{ij}u_{i,k}s_{,j} - (W+K)s_{,k}] dV \tag{21}$$

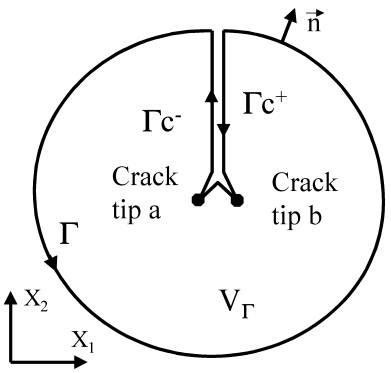

Figure 10 : Integral path for branched crack tips

where Γ is a far-field integral path that encloses all branched crack tips (see Fig. 10) and s is a continuous function defined in V_Γ . When we evaluate the dynamic J integral components at the crack tip a, we set the s function as $s = 1$ for the whole domain except $s = 0$ at the tip b, and vice versa. Equation (21) made it possible to evaluate the dynamic J integral components for interacting branched crack tips.

The crack-axis components of the dynamic J integral for each branched crack tip can be evaluated by the coordinate transformation given by Eq. (16). Then the dynamic stress intensity factors for each branched crack tip can be calculated by the component separation method given by Eqs. (19.a, b) or (20.a, b).

7 Numerical Analyses of Static Branched Cracks

In order to validate the applicability of the switching method of the path independent dynamic J integral explained in the previous section, static analyses are carried out for branched cracks.

Figure 11 shows a doubly symmetric branched crack in an infinite plate under uniform tension. This problem was solved systematically for various branched angles (2θ) and for various branched crack lengths (b) by Vitek (1977) using the dislocation distribution method. The accuracies of the solutions are less than 3% .

Figure 12 shows the numerical analysis model. Due to the symmetry condition, only the right-hand side is modeled. To verify the present generation phase simulation, we employ the same length of straight portion of the branched crack with the experimental one (a=59.54mm) as explained in Section 2. Furthermore, the branched

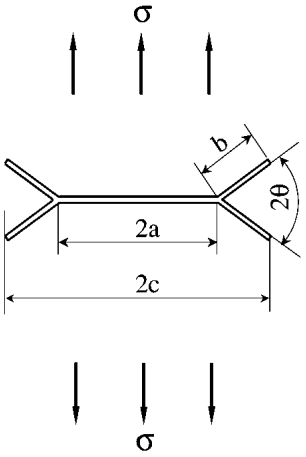

Figure 11 : Static branched crack

angle is set as 2θ=25˚ which is very close to the experimentally observed dynamic crack branching angle (25.2˚). Since the original problem depicted in Fig. 11 was solved for an infinite plate, relatively large height and width compared to the crack length are used in the numerical analysis model, as shown in Fig. 12.

For the static crack problems, the path independent dynamic J integral [Nishioka and Atluri (1983)] reduces to the path independent static J integral [Rice (1968)]. Thus the switching method of path independent dynamic J integral given by Eq. (21) reduces to the following expressions for the switching method of path independent static J integral:

$$J'_k = \int_{\Gamma+\Gamma_c} [W n_k - t_i u_{i,k}] s dS + \int_{V_\Gamma - V_\varepsilon} [-f_i u_{i,k} + \sigma_{ij} u_{i,k} s_{,j} - W s_{,k}] dV. \tag{22}$$

The crack-axis components of the static J integral can be evaluated by the following coordinate transformation:

$$J_l^0 = \alpha_{lk}(\pm\theta) J_k. \tag{23}$$

The tangential component of the static J integral J_1^0 corresponds to the static energy release rate G.

If the energy release rate G or the crack-axis component J_1^0 is obtained by Eq. (23), the mixed-mode static stress intensity factors can be evaluated by the component separation method:

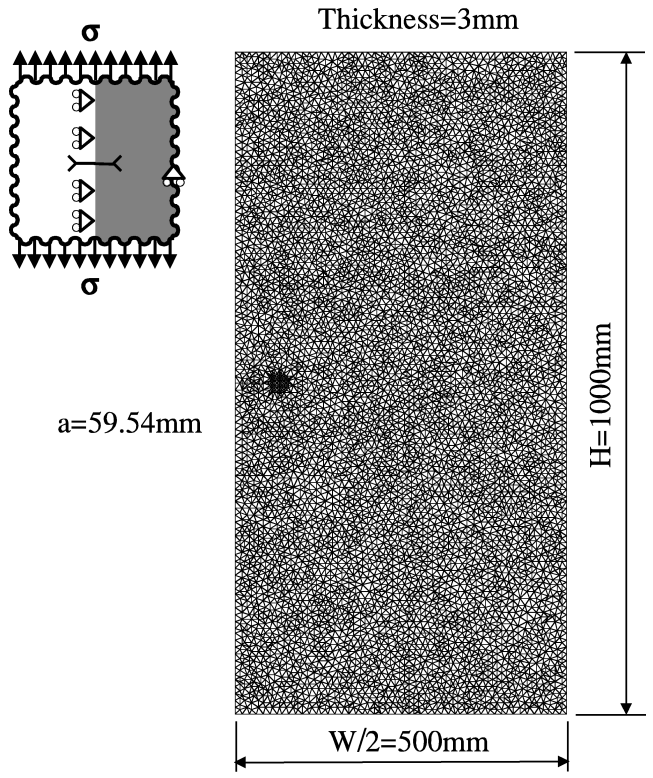

Figure 12 : Numerical analysis model of static branched crack

$$K_I = \delta_I \left\{ \frac{8\mu J_l^0}{(\kappa+1)(\delta_I^2+\delta_{II}^2)} \right\}^{1/2} = \delta_I \left\{ \frac{8\mu G}{(\kappa+1)(\delta_I^2+\delta_{II}^2)} \right\}^{1/2} \tag{24a}$$

$$K_{II} = \delta_{II} \left\{ \frac{8\mu J_l^0}{(\kappa+1)(\delta_I^2+\delta_{II}^2)} \right\}^{1/2} = \delta_{II} \left\{ \frac{8\mu G}{(\kappa+1)(\delta_I^2+\delta_{II}^2)} \right\}^{1/2} \tag{24b}$$

Then the stress intensity factors are normalized as follows:

$$F_I = K_I/\sigma\sqrt{\pi a} \text{ and } F_{II} = K_{II}/\sigma\sqrt{\pi a}. \tag{25}$$

The integral paths for the switching method are shown in Fig. 13. Five paths surrounding both branched crack tips are used. The values of the crack-axis component of the J integral J_1^0 are plotted in Fig. 14 against the integral

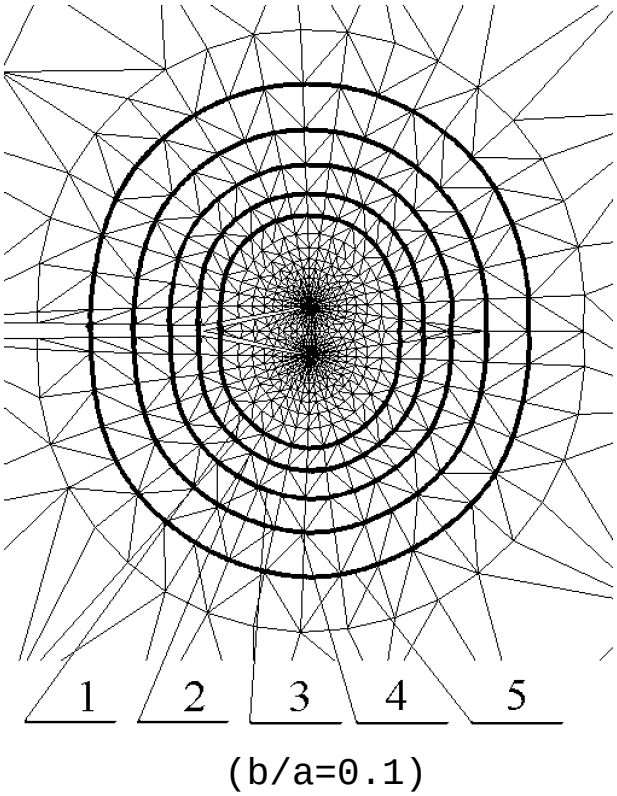

Figure 13 : Integral paths for static branched crack

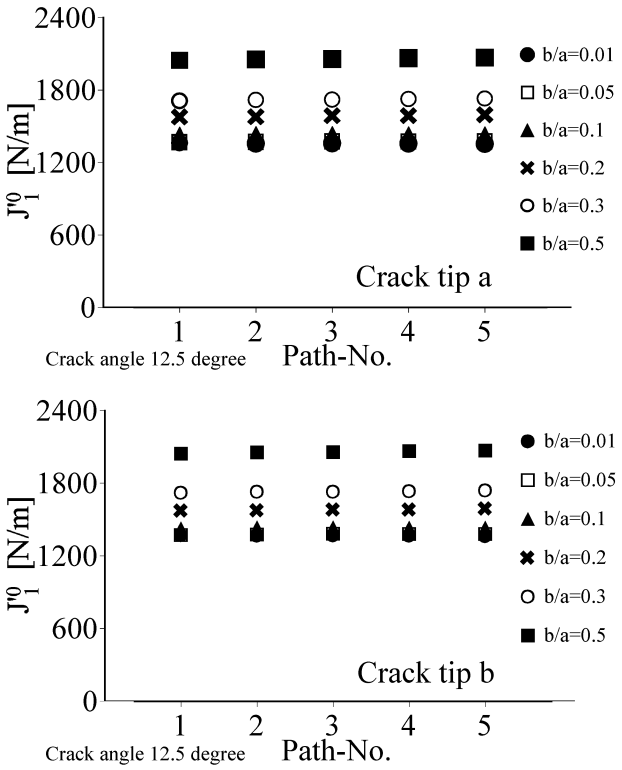

Figure 14 : Path independence of static J integral

path number. The branched crack length is changed from the very shot one (b/a=0.01) to the relatively long one (b/a=0.5). For the cases of b/a=0.01, we set up the static branched crack length shorter than the dynamic branched crack length in the first time step immediately after the onset of the crack branching. For the all cases, excellent path independence can be observed in Fig. 14.

The normalized stress intensity factors obtained by the present method are compared in Fig. 15 with those obtained by the dislocation distribution method [Vitek (1977)]. The present results excellently agree with those of Vitek (1977).

This excellent agreement verifies the applicability of the switching method to branched crack problems.

8 Results of Generation Phase Simulation

Based on the experimental data and the history of dynamic crack branching explained in Section 2, the generation phase simulation was carried out using the moving finite element method. In other words, the dynamic branching fracture phenomenon was regenerated in the

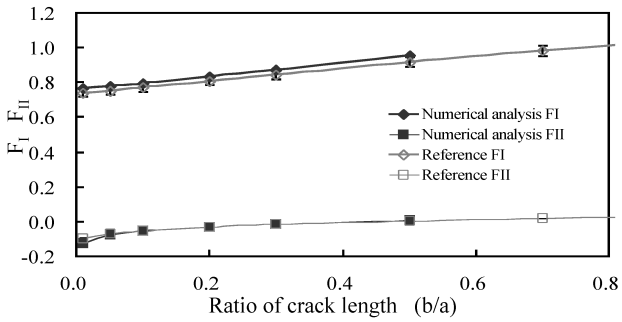

Figure 15 : Comparison the numerical analysis and reference

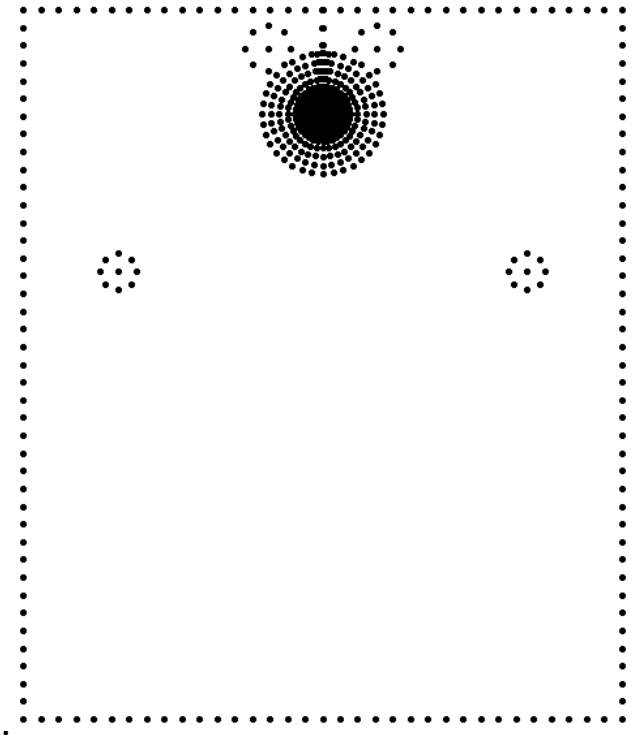

Figure 16 : Input data for automatic mesh generation

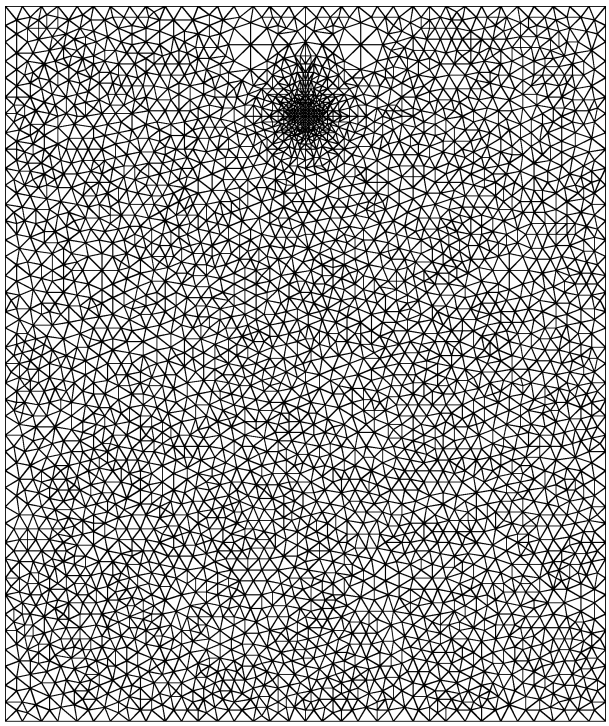

Figure 17 : Initial mesh pattern at t=0

computational model.

The initial mesh pattern was automatically generated by Delaunay automatic triangulation using specified exterior boundary points and specified interior points for the loading pins together with specified interior points around the crack tip (see Fig. 16), which were regularly placed by 15 points in the radial direction and by 10 ° increment in the circumferential direction. The minimum radial increment of 0.15mm was used in the vicinity of the crack tip. Figure 17 shows the automatically generated mesh pattern for the initial state of the specimen. The initial number of elements and the number of nodes were 7414 and 3800, respectively.

Since the steel loading pins were inserted in the loading pin-holes (see Fig. 1), those holes were modeled by steel which has the following material properties: Young's modulus E=206GPa, Poisson's ratio ν=0.28 and mass density ρ=7870kg/m^3.

In the generation phase simulation, first, the experimentally recorded fracture loads of the upper load of 68.6N and the lower load of 1822.8N were applied to the corresponding loading points. After the static analysis under the fracture loads, the displacements at the loading points were evaluated and these were used as the prescribed displacement in the finite element model. The contact and non-contact boundary conditions were applied for the lower loading points during the dynamic fracture simulation.

The time increment of Δt=1.985μs was used. Deformed mesh patterns of the dynamically fracturing specimen are shown in Fig. 18. In order to visualize the crack opening profiles, the deformation was magnified by 10 times. As seen from the figure, the moving finite elements exactly followed not only the dynamically propagating crack tip but also the dynamically branching crack tips.

As stated before, in this simulation, the contact and non-contact conditions on the loading points were considered. Figures 19 and 20 show the time variations of the loads and displacements of loading pins, respectively. The upper loads became zero at about 35μs. Then, the upper loading pins started departing away from the loading jigs. The lower loads gradually decrease to almost zero at the end of the simulation.

The distributions of the stain energy density in the specimen are shown in Fig. 21. At the fracture initiation time (t=0) much higher strain energy density concentra-

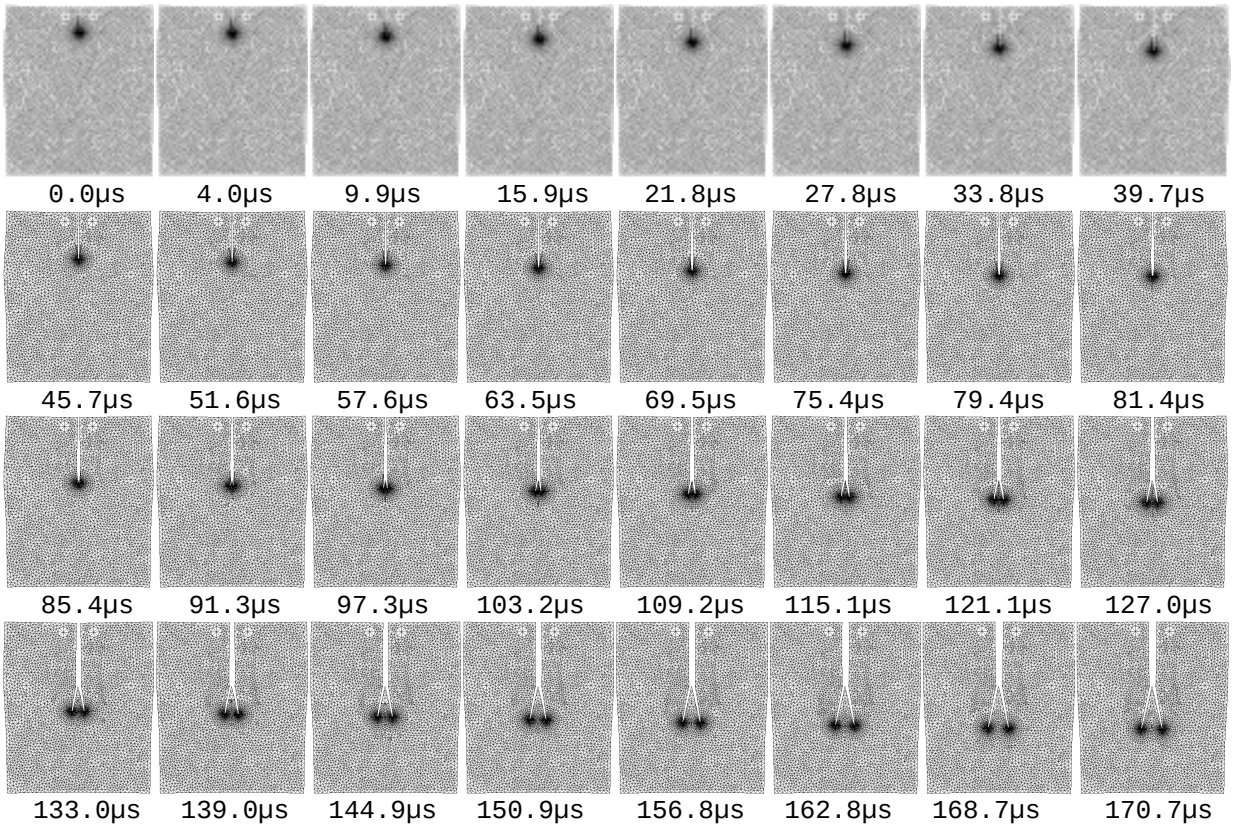

Figure 18 : Generation phase simulation of the dynamic crack bifurcation phenomenon

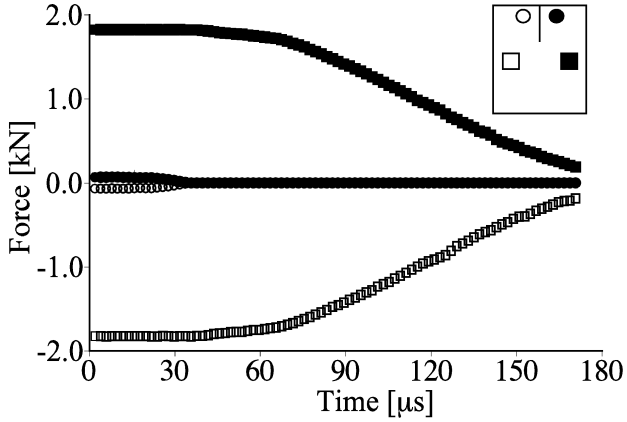

Figure 19 : The time variations of the loads

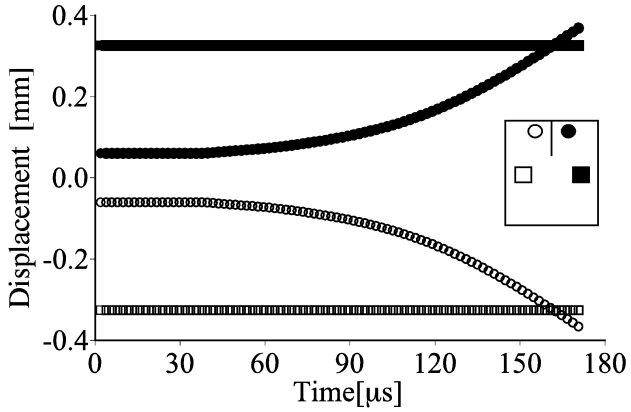

Figure 20 : Displacements of loading pins

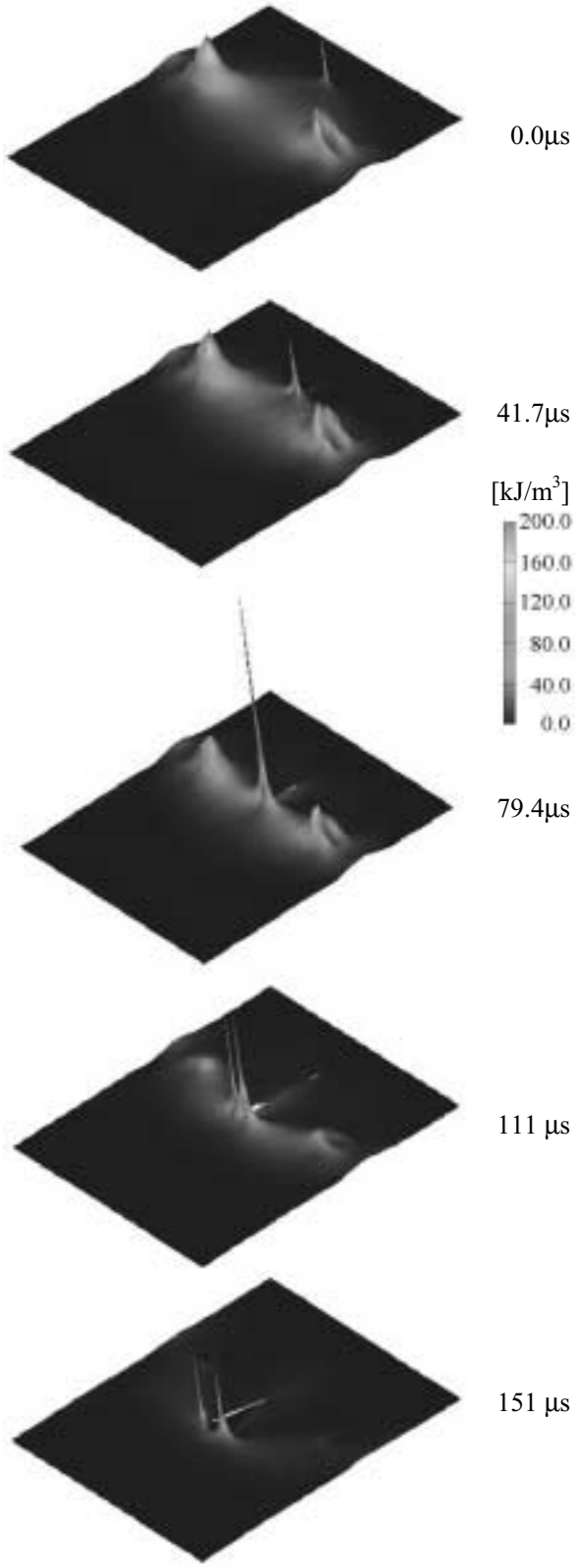

Figure 21 : Strain energy density distribution

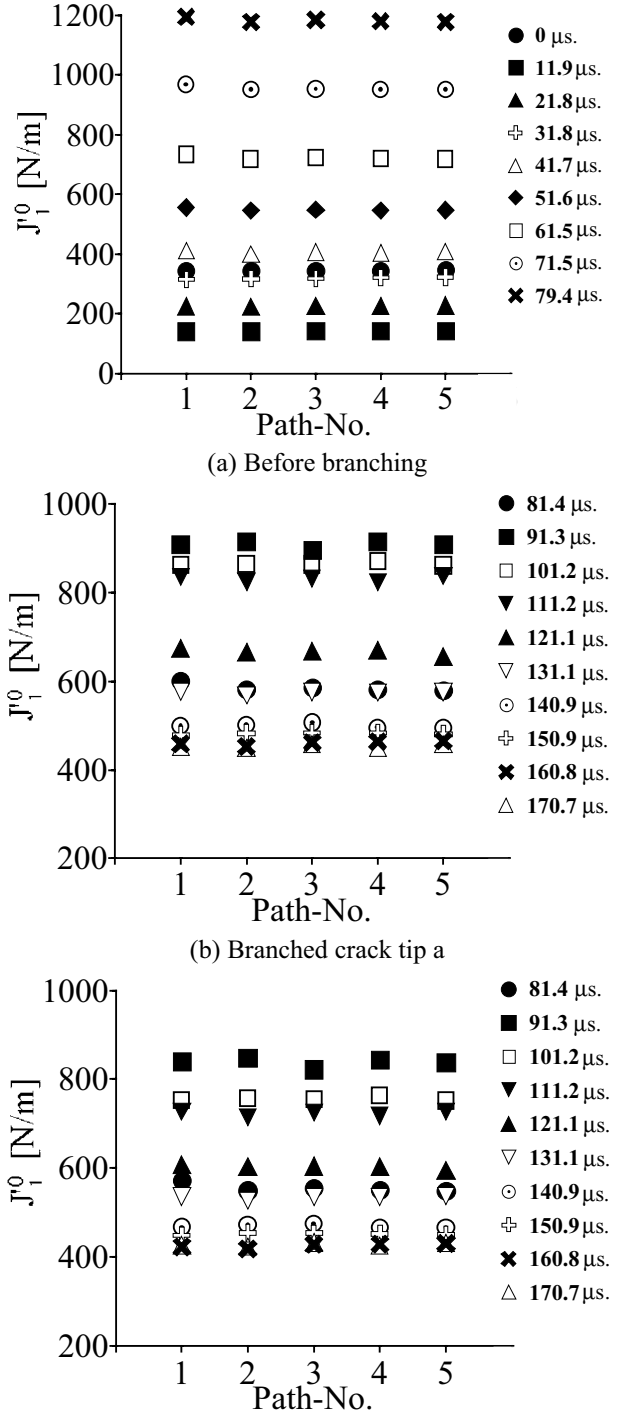

(a) Before branching

(b) Branched crack tip a

Figure 22 : Dynamic J integral against path number (generation phase simulation)

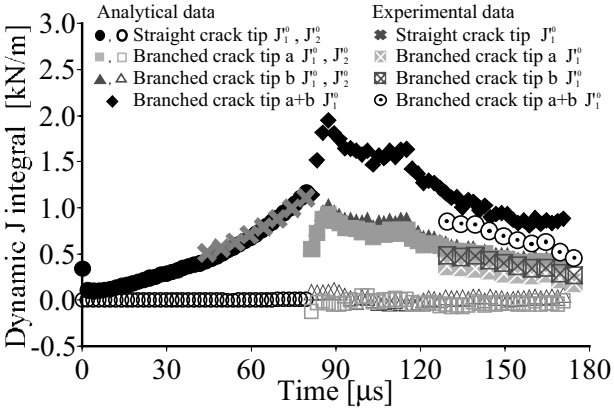

Figure 23 : Variations of dynamic J integral

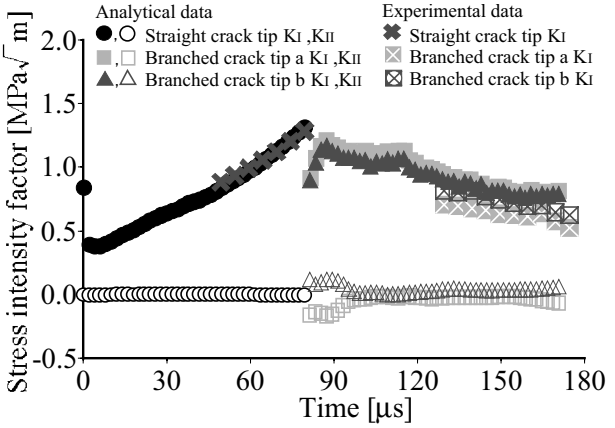

Figure 24 : Variations of K factors

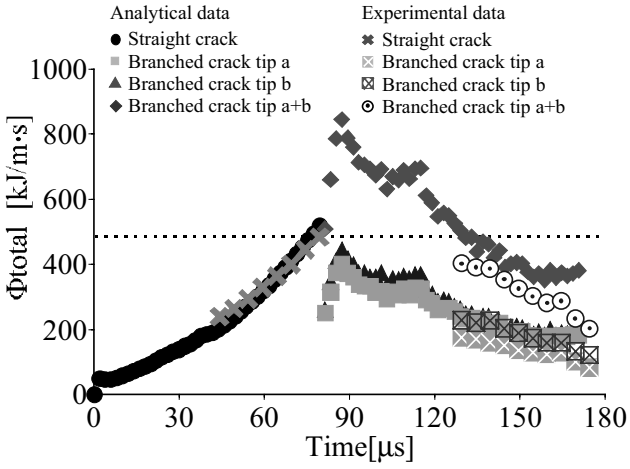

Figure 25 : Variations of energy flux

tions appear around the lower loading points while almost no concentrations appear around the upper loading points. Due to the crack tip singularity, an extremely sharp strain energy density concentration can be seen around the crack tip. The strain energy density concentration at the crack tip becomes the maximum at the crack bifurcation time of t_b=79.4μs. It is made by the strong tensile stress field, which is produced by the lower loading system. After the crack bifurcation, the concentrations around the branched crack tips become smaller when the fracture progresses. At t=151μs, the strain energy density distribution becomes almost flat in the entire specimen, except around two propagating crack tips.

The global components of the dynamic J integral were evaluated for five paths with the radii of 4.883mm, 6.104mm, 7.629mm, 9.537mm and 11.444mm. Then, the dynamic J values were converted to the crack-axis components. The values of the crack-axis component of the dynamic J integral for the single crack tip and the branched crack tips are plotted in Fig. 22 against the path number. In all cases, the dynamic J integrals are excellently path independent.

The time variations of the dynamic J integrals before and after crack bifurcation are shown in Fig. 23. The simulation results agree well with experimental results obtained by the method of caustics [Nishioka, Kishimoto, Ono and Sakakura (1999a, 1999b)]. In this paper, the elasto-optical constant of C_0= -1.05$\times 10^{-10}$ [m/N] was used, while C_0= -1.20$\times 10^{-10}$ [m/N] was used in [Nishioka, Kishimoto, Ono and Sakakura (1999a, 1999b)]. The sum of the dynamic J integrals for branched crack tips is also shown in the figure. The total dynamic J integral, i.e., the total energy release rate is continuous immediately before and after the crack bifurcation.

The dynamic stress intensity factors are plotted in Fig. 24. The numerical results agree well with the experimental K values obtained by the method of caustics. At the branched crack tips, the mode II stress intensity factors reduce to almost zero, except in the early stage after the crack bifurcation.

The energy flux to the propagating crack tip per unit time was calculated by $\Phi_{total}= J' \cdot C$, and plotted in Fig. 25. In the experimental study [Nishioka, Kishimoto, Ono and Sakakura (1999a, 1999b)], we have clarified the mechanism of crack bifurcation, based on the fact that the crack bifurcation occurs when the energy flux reaches a critical value of the material. It can be seen that the energy flux reaches the maximum value at the crack bifurcation time (t_b=79.4μs). The energy flux for each branched crack is smaller than this critical value. This implies that no further bifurcation occurs from the either of branched crack tips.

9 Conclusions

In this study, important key technologies were developed for the numerical simulation of dynamic crack bifurcation phenomenon. These are the moving finite element method based on Delaunay automatic triangulation and the switching method of the path independent dynamic J integral for branched cracks. The switching method made it possible to evaluate various fracture parameters for dynamically branching crack tips.

Using the presently developed key technologies, the generation phase simulation of the dynamic crack bifurcation phenomenon in Homalite-911 was carried out. The fracture mechanics parameters were successfully obtained even immediately after the crack bifurcation, where it was difficult to do by the experiment. The simulated results agreed excellently with the experimental ones. The numerical results also proved that the total energy release rate and the total energy flux are continuous immediately before and after the crack bifurcation.

Acknowledgement: This study was supported by the Grant-in-Aid for Scientific Research (No.08455063) from the Ministry of Education, Science and Culture in Japan, and also by the natural science grant from Mitsubishi Foundation.

References:

Abraham, F.F. (2000): MAADLY spanning the length scales in dynamic fracture. *CMES: Computer Modeling in Engineering & Sciences*, vol.1, no.4, pp.63-70.

Bathe, K.J.; Wilson, E.L. (1976): *Numerical methods in finite element analysis*. Prentice-Hall, New Jersey.

Chen, Z.; Hu, W.; Chen, E.P. (2000): Simulation of dynamic failure evolution in brittle solids without using nonlocal terms in the strain-stress space. *CMES: Computer Modeling in Engineering & Sciences*, vol.1, no.4, pp.57-62.

Ching, H-K.; Batra, R.C. (2001): Determination of crack tip fields in linear elastostatics by the meshless

local petrov-galerkin (MLPG) method. *CMES: Computer Modeling in Engineering & Sciences*, vol.2, no.2, pp.273-290.

Kanninen, M.F. (1978): A critical appraisal of solution techniques in dynamic fracture mechanics. In: D.R.J. Owen and A.R. Luxmoore (eds) *Numerical methods in fracture mechanics*, Pineridge Press, pp.612-634.

Kim, H.G.; Atluri, S.N. (2000): Arbitrary placement of secondary nodes, and error control, in the meshless local petrov-galerkin (MLPG) method. *CMES: Computer Modeling in Engineering & Sciences*, vol.1, no.3, pp.11-32.

Nishioka, T. (1994): The state of the art in computational dynamic fracture mechanics. *JSME International Journal*, Series A, vol.37, pp.313-333.

Nishioka, T. (1997): Computational dynamic fracture mechanics. *International Journal of Fracture*, vol.86, no.1/2, pp.127-159.

Nishioka, T.; Atluri, S. N. (1982): Finite element simulation of fast fracture in steel DCB specimen. *Engineering Fracture Mechanics*, vol.16, no.2, pp.157-175.

Nishioka, T.; Atluri, S.N. (1983): Path independent integrals, energy release rates and general solutions of near-tip fields in mixed-mode dynamic fracture mechanics. *Engineering Fracture Mechanics*, vol.18, no.1, pp.1-22.

Nishioka, T.; Perl, M.; Atluri, S.N. (1983): An analysis of dynamic fracture in an impact test specimen. *Journal of Pressure Vessel Technology*, vol.105, no.2, pp.124-131.

Nishioka, T.; Atluri, S.N. (1986): Computational methods in dynamic fracture, In: S.N. Atluri (ed) *Computational methods in the mechanics of fracture*, Elsevier Science Publishers, pp.336-383.

Nishioka, T.; Kishimoto, T.; Ono, Y.; Sakakura, K. (1999a): Basic studies on the governing criterion for dynamic crack branching phenomena. *Transactions of the Japan Society of Mechanical Engineers*, vol.65, no.633, Ser. A, pp.1123-1131.

Nishioka, T.; Kishimoto, T.; Ono, Y.; Sakakura, K. (1999b): Governing criterion of dynamic crack bifurcation. In: F. Ellyin and J.W. Provan (eds.) *Progress in mechanical behaviour of materials*, Volume I, pp.255-260.

Nishioka, T.; Tokudome, H.; Kinoshita, M.; Nishida, H. (1998): Dynamic fracture path prediction by moving finite element method based on Delaunay automatic triangulation. *Modeling and simulation based engineering*, vol. II, Tech Science Press, pp.1335-1340.

Nishioka, T.; Tokudome, H.; Kinoshita, M. (2001): Dynamic fracture-path prediction in impact fracture phenomena using moving finite element method based on Delaunay automatic mesh generation. *International Journal of Solids and Structures*, vol. 38, no.30-31, pp.5273-5301.

Rice, J.R. (1968): A path independent integral and approximate analysis of strain concentration by notches and cracks. *Journal of Applied Mechanics*, vol.35, pp.379-386.

Sloan, S.W.; Houlsby, G.T. (1984): An implementation of Watson's algorithm for computing two-dimensional Delaunay triangulation. *Advances in engineering software*, vol.6, pp.192-197.

Taniguchi, T. (1992): *Automatic mesh generation for FEM: use of Delaunay triangulation.* Morikita Publishing.

Vitek, V. (1977): Plane strain stress-intensity factors for branched cracks. *International Journal of Fracture*, vol. 13, no.4, pp.481-501.